J. Fluid Mech. (2009), *vol.* 632, *pp.* 301–327.
doi:10.1017/S0022112009007198 Printed in the United Kingdom

Drop impact of yield-stress fluids

LI-HUA LUU AND YOËL FORTERRE†

Laboratoire IUSTI, CNRS UMR 6595, Aix-Marseille Université, 5 rue Enrico Fermi, 13453 Marseille Cedex 13, France

(Received 13 November 2008 and in revised form 18 March 2009)

The normal impact of a drop of yield-stress fluid on a flat rigid surface is investigated experimentally. Using different model fluids (polymer microgels, clay suspensions) and impacted surfaces (partially wettable, super-hydrophobic), we find a rich variety of impact regimes from irreversible viscoplastic coating to giant elastic spreading and recoil. A minimal model of inertial spreading, taking into account an elasto-viscoplastic rheology, allows explaining in a single framework the different regimes and scaling laws. In addition, semi-quantitative predictions for the spread factor are obtained when the measured rheological parameters of the fluid (elasticity, yield stress, viscosity) are injected into the model. Our study offers a means to probe the short-time rheology of yield-stress fluids and highlights the role of elasticity on the unsteady hydrodynamics of these complex fluids. Movies are available with the online version of the paper (go to journals.cambridge.org/flm).

1. Introduction

Yield-stress fluids (e.g. mud, pastes, emulsions) are often modelled, from a fluid mechanical point of view, using simple steady flow rules such as the Bingham or Herschel–Bulkley model (Balmforth & Frigaard 2007). However, these constitutive laws are usually a significant simplification of their true rheological behaviour, which may display elasticity, ageing, shear localization, wall slip and the like (Barnes, Hutton & Walters 1989; Pignon, Magnin & Piau 1996; Meeker, Bonnecaze & Cloitre 2004; Coussot 2005). The extent to which such rheological features affect the hydrodynamics of yield-stress fluids in complex configurations remains an important issue for many applications. The objective of the present paper is to study the dynamics of a drop of yield-stress fluid impacting a solid surface. This configuration provides an unusual test for the rheology, as it involves large deformations and highly elongational flows on short time scales. Our main intent is to get insight into the short-time behaviour of yield-stress fluids, in flow conditions difficult to achieve with conventional rheometers.

Drop impact dynamics on solid surfaces is a classical subject of interfacial hydrodynamics, which occurs in many industrial and environmental situations such as inkjet printing, coating, motor jet, rain drop and pesticides (Rein 1993; Yarin 2006). The most recent research on this subject is directed towards the understanding of fingering instabilities and the splashing transition (Thoroddsen & Sakakibara 1998; Xu, Zhang & Nagel 2005), the receding and bouncing dynamics on super-hydrophobic surfaces (Renardy *et al.* 2003) or the direct three-dimensional numerical modelling (Rieber & Frohn 1999; Bussmann, Chandra & Mostaghimi 2000). So far, most of

† Email address for correspondence: yoel.forterre@polytech.univ-mrs.fr

the studies have concerned Newtonian fluids. More recently, non-Newtonian effects (e.g. normal stresses, elasticity) have also been investigated by adding polymers or surfactants in the fluid (Cooper-White, Crooks & Boger 2002; Bartolo *et al.* 2007). However, in some practical circumstances, the fluid used is more complex and may display a flow threshold: at low stresses the fluid behaves like a solid, but above a critical stress, it yields and flows. A few examples are spray painting and inkjet printing of three-dimensional structures, using colloidal gels (Lewis 2006). On the other hand, the study of impacts of yield-stress fluids may be regarded as a laboratory model for investigating high-speed collision of solids, such as ballistic impact (Yarin, Rubin & Roisman 1995), impact crater formation (Melosh 1989) and explosive welding (Crossland 1982). In this case, an important parameter is the ratio of the impacting dynamic pressure ρV_0^2 (ρ is the object density and V_0 is the impacting velocity) to the material yield stress τ_c (Johnson 1985). Since typical yield-stress fluids (gels, clays, emulsions) have strengths millions of times below those of metals or soils (few tens of Pa compared to few tens of MPa), their impact at low velocities ($V_0 \sim \mathrm{m\,s^{-1}}$) could mimic the extreme collision speeds ($V_0 \sim \mathrm{km\,s^{-1}}$) for which the classical solid flows (Awerbuch & Bodner 1974).

To date, there have been very few controlled studies of drop impacts involving threshold fluids. In a recent paper, Nigen (2005) has investigated the spreading dynamics of droplets of Vaseline impacting a smooth Plexiglas surface. However, the experimental conditions were such (small drop diameter, high viscosity, low yield stress) that viscous effects mostly dominated the spreading dynamics. Yet, an interesting observation was that the yield stress could inhibit the capillary recoil and 'freeze' the drop shape at its maximal deformation. This suggests that, unlike Newtonian fluids, the impact dynamics of a yield-stress fluid may be mainly controlled by its intrinsic rheology rather than by capillary effects or surface wetting properties.

To test this, we will study drop impacts of yield-stress fluids for a wide range of rheological parameters (elasticity, yield stress, viscosity) and impacted surfaces (partially wetting, super-hydrophobic). We will mainly focus on the physical mechanisms that control the maximal spread factor, defined as the maximal drop extension during the impact L_m divided by the drop initial size L_0. For Newtonian fluids, empirical scaling laws have been proposed, depending on whether the initial kinetic energy is mostly converted into surface energy or dissipated by viscosity (Chandra & Avedisian 1991; Clanet *et al.* 2004). For yield-stress fluids, two obvious complications arise. First, the existence of a threshold introduces an additional plastic-like dissipation mechanism. Second, these fluids usually display a non-Newtonian shear-rate-dependent viscosity, which should modify the classical viscous-spreading laws.

A more complex issue concerns the role of the elastic deformations in the spreading dynamics. For most flow problems involving yield-stress fluids, elasticity is neglected as soon as the material is above the flow threshold. However, this is far from being obvious in the case of impacting drops in which highly time-dependant and elongational flows are considered. This interplay between flow, elasticity and viscosity is well known in polymer fluid mechanics (Bird, Armstrong & Hassager 1987) but has been less investigated for yield-stress fluids. Recently, elasto-viscoplastic constitutive laws have been proposed that consistently take into account this coupling for soft disordered materials such as foams, emulsions and polymer pastes (Takeshi & Sekimoto 2005; Marmottant & Graner 2007; Saramito 2007; Bénito *et al.* 2008). They have proven promising in capturing interesting features of soft viscoplastic fluids such as normal stress, transient flows and localization in Couette geometries (Cheddadi *et al.* 2008).

In this paper, we gain from these approaches to understand, within a single framework, the different regimes and scaling laws that control the drop impact dynamics of a yield-stress fluid. We first present the experimental set-up and yield-stress fluids used in § 2. The different impact regimes observed on partially wetting and super-hydrophobic surfaces are presented in § 3. We show that elasticity may play a crucial role in the spreading dynamics, even when the drop deformations are far above the flow threshold. To explain this observation, a minimal temporal model of spreading is built, where drop inertia is balanced by an elasto-viscoplastic basal stress (§ 4). The comparison between experiments and the simplified model is given in § 5, focusing more specifically on the maximal spread factor. A discussion and some questions raised by this study are given in the conclusion (§ 6).

2. Experimental methods

2.1. *Yield-stress fluids*

Three different kinds of yield-stress fluids were used to perform the experiments: two colloidal suspensions of clay (kaolin and bentonite; van Olphen 1977) and one polymer micro-gel suspension (Carbopol dispersion; Oppong *et al.* 2006; Piau 2007). These fluids are known to present a yield stress above a critical concentration and are widely used as model viscoplastic fluids in the literature (Coussot 1994; Osmond & Griffiths 2001; de Bruyn, Habdas & Kim 2002; Peixinho *et al.* 2005; Tabuteau, Coussot & de Bruyn 2007; Chambon, Ghemmour & Laigle 2008). In addition, they allow spanning a broad range of mechanical and rheological parameters by changing the concentration of the suspension. In the following, we will focus on the elastic and viscoplastic properties of clays and Carbopol suspensions. We will disregard other rheological features that may affect these fluids close the flow threshold, such as creeping, thixotropy and microstructural orientation effects (Pignon, Magnin & Piau 1997; Coussot 2005; Piau 2007). We will see that the knowledge of the elasto-viscoplastic parameters indeed is sufficient to describe the main features of the drop impact dynamics observed in our experiments.

The slurries of kaolin (supplied by Miniere Kaolins Morbihan, France) and bentonite (supplied by VWR Prolabo) were prepared by gradually adding a given mass of clay powder with de-ionized water under continuous and active mixing. The suspensions were then stored for 72 h to ensure a complete hydration and dispersion of the clay particles. Prior to any test, the slurries were mixed again for 1 h. Note that, compared to kaolin, benonite suspensions are strongly thixotropic, meaning that their mechanical properties (elasticity, yield stress) evolve at rest. In this study, we used two different concentrations of kaolin and bentonite suspensions (see table 1, where the weight percentage gives the ratio between the total mass of particles to the total mass of particles and water initially mixed). Carbopol dispersions (Carbopol ETD 2050 supplied by Noveon) were prepared by adding slowly Carbopol powder into de-ionized water at 50°C, under continuous stirring during several hours at 500 rpm. Sodium hydroxide solution at 18 % was then progressively added to bring the pH up to 7. A post-mixing at 700 rpm during 9 h was required to eliminate lumps and air bubbles, resulting in a transparent gel. For the experiments, we used six different concentrations of Carbopol from 0.2 % to 3 % in weight (see table 1). In all cases, the final suspension density was measured by weighting 10 syringes of 30 ml accurately filled with the fluid (table 1; accuracy better than 1 %). Finally, the surface tension σ of the fluids, which are aqueous dispersions without any surfactant, was assumed to be equal to that of pure water, $\sigma = 0.07$ N m^{-1}. We did not determine directly the surface

Fluid	Weight (%)	τ_c (Pa)	K (Pa s^n)	n	G (Pa)	G'' (Pa)	ρ (kg m^{-3})	L_0 (mm)	D (mm)
Carbopol									
C02	0.2	3.9	3.2	0.50	28	5.0	1010	7.6	8
C035	0.35	8.4	5.1	0.50	47	7.3	1010	8.0	8
C05	0.5	14	8.0	0.50	61	8.9	1020	8.7	8
C1	1	24	11	0.50	85	12	1020	12	12
C2	2	52	18	0.50	135	21	1020	17.5	17
C3	3	92	32	0.50	270	36	1020	25	27
Bentonite									
B13	13	68	0.12	0.96	2400	60	1090	16	14
B15	15	124	0.16	0.96	3800	120	1090	29.5	27
Kaolin									
K51	51	50	36	0.36	37 000	6500	1630	20	20
K55	55	91	68	0.36	200 000	69 000	1630	26.5	27

TABLE 1. Properties of the fluids, drop size L_0 and syringe diameters D.

tension because most measurement methods are corrupted by the fluid yield stress and elasticity. However, recent measurements in agar gels using surface-deformation spectroscopy confirm that the surface tension of aqueous gels is close to (but slightly lower than) that of water (Yoshitake *et al.* 2008). The value $\sigma = 0.07\,\mathrm{N\,m^{-1}}$ should therefore be taken as an upper bound for the real surface tension of our fluids.

Bulk rheological measurements of each fluid were made in a rotational Anton Paar MCR 501 controlled-stress rheometer. The samples were contained within a plate-and-cone geometry 5 cm in diameter. The tool surfaces were roughened to minimize wall slip, and special care was taken to avoid evaporation during the tests (Magnin & Piau 1990). We performed both steady-state shear and oscillatory measurements. In the steady-state measurements, the shear stress τ was measured as function of the applied shear rate $\dot{\gamma}$, by decreasing the shear rate step-by-step in the range 10^{-1}–10^3 s^{-1} and averaging the measured shear stress over 100 s. In the oscillatory measurements, a small sinusoidal shear strain was applied and the resulting shear stress measured. The in-phase and out-of-phase components of the response give the elastic shear modulus G and the viscous loss modulus G'', respectively.

Figure 1 presents typical steady-state flow curves for the three kinds of fluids. Each point represents an average over two samples (see § 2.2). We observe that all fluids display a yield stress and are shear-thinning above the flow threshold. The flow curves are fairly well represented by a Herschel–Bulkley model: $\tau = \tau_c + K\dot{\gamma}^n$, where τ_c is the fluid yield stress, K the fluid consistency and n the flow index (Barnes *et al.* 1989). For bentonite, the Herschel–Bulkley model is less accurate, especially at low shear rates at which the stress appears to increase when the shear rate decreases. This stress minimum in the flow curve has been documented before and is likely related to the thixotropic nature of this fluid, which may cause flow inhomogeneities inside the sample at low shear rates (Pignon *et al.* 1996). Determinations of the Herschel–Bulkley parameters were obtained using a nonlinear parameter fitting, by fixing the value of n for each fluid. For bentonite, only the monotonic part of the flow curve has been fitted. We have checked that fitting the whole flow curve only results in small changes of the rheological parameters that do not modified the main results of the study. Values of the rheological parameters obtained for all fluids are

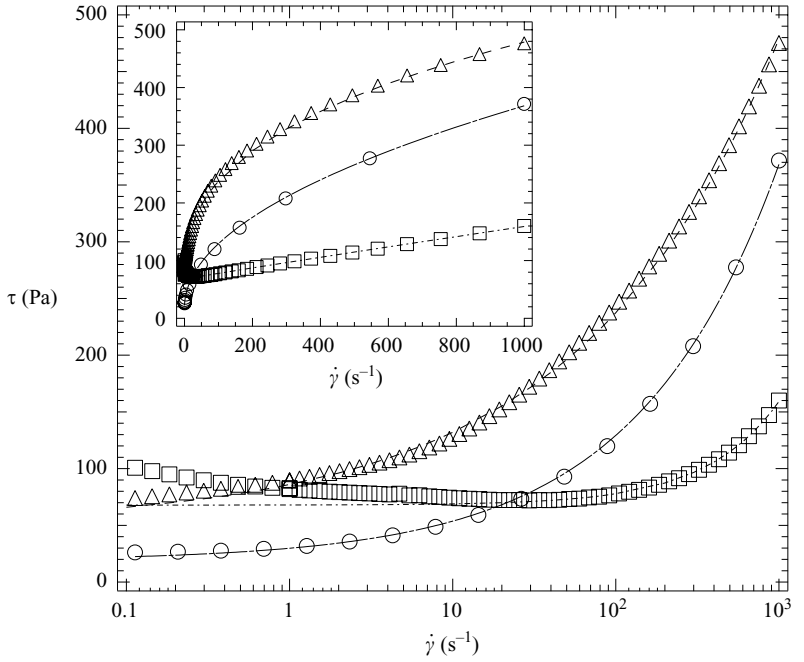

FIGURE 1. Examples of steady-state flow curves for each fluid in semi-log coordinates: kaolin 51 % (△), Carbopol 1 % (○), bentonite 13 % (□). The continuous lines give the Herschel–Bulkley fit (see table 1). Inset: same data in lin–lin coordinates.

collected in table 1. As expected, both the yield stress and the consistency increase with the material concentration. All fluids show a similar yield stress, bentonite being less 'viscous' than kaolin and Carbopol. Note that the overall uncertainty on τ_c and K is about 10 % due to material reproducibility and fitting procedure.

The elastic shear modulus G obtained from the oscillatory measurement is also given in table 1. It was shown to depend only weakly on the applied frequency (in the range 0.1–10 Hz) and strain amplitude, up to a critical strain γ_c corresponding to the flow threshold. Below the threshold, we may thus assume the shear modulus constant for each fluid and define the critical strain by $\gamma_c \equiv \tau_c/G$. Both the shear modulus and critical strain strongly depend on the material. Carbopol is very soft and typically remains elastic up to 25 % strain, whereas bentonite is more rigid and starts to flow above 3 % strain. The kaolin slurry is the most rigid material with a critical strain less than 0.1 %. Values for G in table 1 are obtained at frequency 1 Hz and amplitude strain 1 % (Carbopol) or 0.01 % (kaolin, bentonite). Uncertainties for G are about 7 % for Carbopol and 20 % for kaolin and bentonite. Note that below the flow threshold, the loss modulus G'' for all fluids was 3–40 times smaller than the elastic shear modulus, showing that these materials are essentially elastic at low stresses (table 1; the values for the loss modulus are given at the same strain amplitudes and frequency than for the elastic modulus).

In the following, we will use the mechanical and rheological properties given in table 1 to analyse our impact experiments. However, for complex fluids, it is not obvious *a priori* that parameters deduced from simple shear flows are sufficient to describe more complex flow configurations such as drop impacts, which involve both shear and elongational flows. We have not performed elongational measurements of

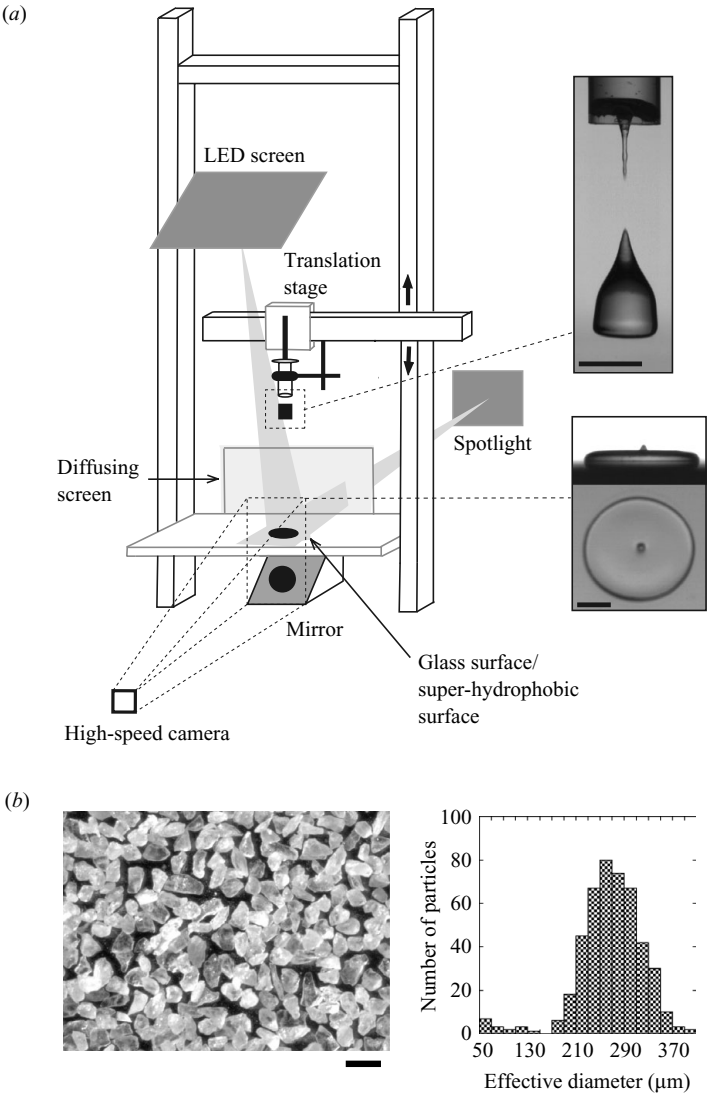

FIGURE 2. (*a*) Sketch of the experimental set-up and typical image obtained on the smooth glass surface. Scale bars, 12 mm. (*b*) Close-up view of the super-hydrophobic surface, made by gluing one layer of hydrophobic sand on the glass plane. The plot gives the distribution over 460 sand particles of the effective diameter, defined as $\sqrt{4a/\pi}$, where a is the projected area of the grain. Scale bars, 0.4 mm.

our fluids. However, several studies on clays and Carbopol suggest that rheological parameters measured in simple shear and uniaxial extension closely agree for these yield-stress fluids (O'Brien & Mackay 2002; Yarin *et al.* 2004; Mohamed Abdelhaye, Chaouche & Van Damme 2008).

2.2. *Impact experimental set-up*

The experimental set-up of drop impact is sketched in figure 2(*a*). Drops are slowly extruded from a cut plastic syringe (inner diameter $D = 8-27$ mm), using a motorized translation stage (1 mm s^{-1}). After a fall height 1–145 cm (giving an impacting velocity

$V_0 = 0.4-5.6$ m s^{-1}), drops impinge on to a 1 cm thick and 50 cm wide rigid horizontal glass plate. The impact dynamics are visualized using a high-speed camera (Photron Fastcam APX RS, 5000 Hz, 512×1024 pixels) with a microlens (Sigma 24–70 mm 1:2.8 EX DG). An inclined mirror settled under the glass surface allows monitoring both the side and bottom views at the same time. The drop is backlighted using an LED lighting screen (Phlox) and a 500 W spotlight through a diffusing paper. A typical image obtained with Carbopol 1 wt % is shown in figure 2(*a*). From the bottom view, the instantaneous drop's contact area $A(t)$ is extracted using standard threshold and edge-detection algorithms (software ImageJ, http://rsbweb.nih.gov/ij/).

It is worth noting that in most experiments the Laplace pressure due to the surface tension σ/D is small compared to the fluid yield stress τ_c. In this case, the shape and size of the extruded drop are not controlled by the surface tension but given by a complex balance between gravity, yield stress and extrusion speed (Coussot & Gaulard 2005), resulting in bottle-shaped drops (figure 2*a*). To define the initial drop size L_0, we thus averaged over 20 launches the drop weight m and defined L_0 as the diameter of the equivalent sphere of same volume: $L_0 \equiv (6m/\pi\rho)^{1/3}$ (table 1; the dispersion for each value ranges from 3 % to 13 %). Note that this quantity gives no information about the drop shape. In all the experiments, we have adjusted for each fluid the syringe diameter D, in order to get an aspect ratio L_0/D always close to 1 (table 1).

We performed experiments using two kinds of impacted surfaces: a partially wetting surface and a super-hydrophobic surface. The partially wetting surface was made of smooth float glass, with a water static contact angle of about 42°. The super-hydrophobic surface was made by gluing one layer of hydrophobic sand (supplied by the toys fabricant Tobar under the name 'Underwater Sculpting Sand') with a transparent spray on the glass surface (figure 2*b*). The sand-grain size distribution measured with a digital imaging system was observed to be approximately Gaussian with a mean effective diameter of 265 ± 55 μm (the error corresponds to the standard deviation; see figure 2*b*). The compactness of the glued granular layer, defined as the ratio between the projected area of the grains to the total area, was about 0.8 ± 0.05. The resulting textured surface was highly hydrophobic with a water contact angle close to 180°. It was also highly non-adhesive for all the yield-stress fluids used.

In this study, we adopted the following procedure in order to obtain reproducible measurements: First, to restrain structural ageing and/or external contamination, fluids were used by the week following their making and thoroughly mixed before the experiments. Their rheological properties were then averaged before and after each set of experiments, with typical fluctuations less than 10 %. Finally, for experiments with bentonite, which is thixotropic, suspensions were mixed and allowed to rest 1 min before filling the syringe and releasing the drop. Note that we did not change the resting time before the experiments systematically. The main effect of increasing the resting time is to increase the stress needed to start the flow and hence to modify the size and shape of the extruded bentonite drop (Coussot & Gaulard 2005). The interplay between this ageing and the rapid fluid rejuvenation during the impact is an interesting question that we leave for future studies.

3. Main observations

3.1. *Spreading dynamics and maximal drop deformation*

Typical impact regimes observed with Carbopol drops on the smooth glass surface are shown in figure 3, where the impact velocity increases from top to bottom.

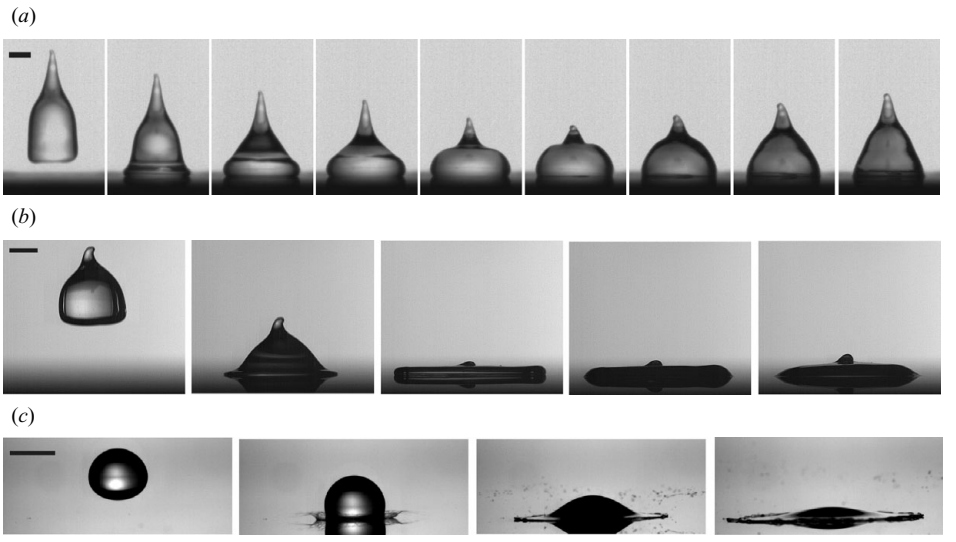

FIGURE 3. Typical impact sequences on a glass surface with Carbopol drops: (*a*) 1 wt%, $V_0 = 0.5$ m s^{-1}; (*b*) 1 wt%, $V_0 = 2.1$ m s^{-1}; (*c*) 0.2 wt%, $V_0 = 4.3$ m s^{-1}. Time interval between the pictures: (*a*) 4 ms, (*b*) 5.6 ms, (*c*) 0.7 ms. Scale bars, 5 mm.

At low velocities, the drop only weakly deforms, and one observes elastic ringing waves propagating along the free surface after the impact (figure 3*a*). For higher velocities, the drop spreads out radially along the surface. A thin liquid layer first jets out sideways from beneath the drop, while the rest of the drop keeps collapsing downward. After a few ms, the drop shape takes the form of a flattened disc that continues to spread until it reaches a maximal diameter L_m (figure 3*b*). The free surface of the drop then flows back and oscillates, while the contact line remains anchored to the plane (figure 3*b*). Note that for kaolin and bentonite, similar behaviours are observed, except that the drops abruptly 'freeze' as soon as they reach their maximal deformation. Finally, for the largest velocities and/or lowest fluid concentrations, the spreading lamella may undergo a front instability that eventually yields to a splash of the drop (figure 3*c*). For Newtonian fluids, the splashing transition is complex and depends on many features such as surface roughness, wetting properties, fluid viscosity and even surrounding gas pressure (Rein 1993; Yarin 2006). Understanding this transition for yield-stress fluids is beyond the scope of this study. In the following, we rather focus on the stable spreading regime, where the drop has an axisymmetric shape. Note that in some cases, a slight asymmetry of the spreading layer is observed because the drop is tilted when impacting the surface (see for example figure 6). This initial inclination may promote the splashing transition but does not modify the spread factor. In the following, the instantaneous spread diameter of the drop $L(t)$ will be accurately computed by $L(t) \equiv \sqrt{4A(t)/\pi}$, where $A(t)$ is the measured drop's contact area from below.

Although the spreading scenario is common to all fluids used, the maximal extent reached by an impinging drop does depend on the fluid characteristics and not only on the impact velocity. Figure 4 presents the maximal spread factor, L_m/L_0, as a function of impact velocity V_0 for all fluids, drop sizes and impacted surfaces studied. The maximal spread factor varies from approximately 1.2 to 6 for the velocity range investigated. For a given material and velocity, the spread factor tends to decrease

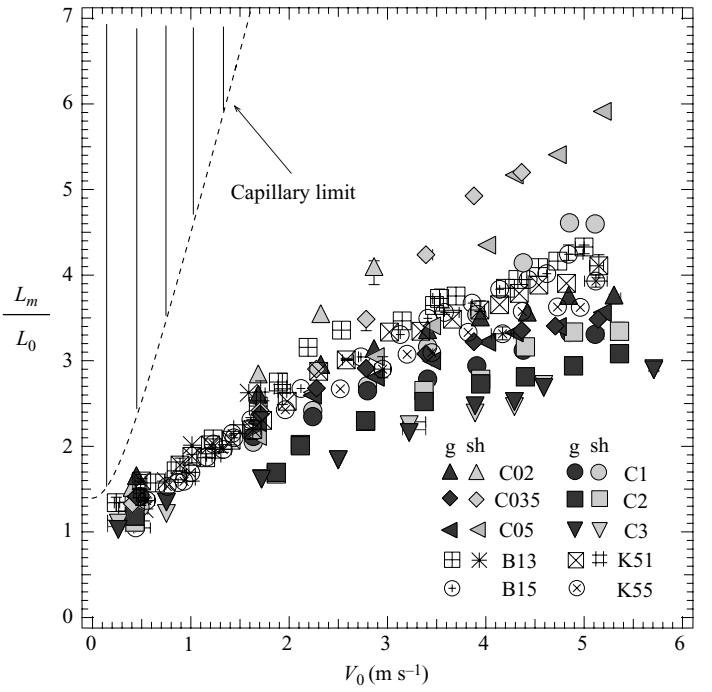

FIGURE 4. Maximal spread factor as a function of impact velocity for all fluids and impacted surfaces investigated: g, glass smooth surface; sh, super-hydrophobic surface. The error bars represent the dispersion over three drops. The dotted line gives a lower bound for the maximal spread factor limited by capillarity: $L_{max}/L_0|_{cap} = [(4 + We/3)/(1 - \cos\theta)]^{1/2}$, where $We = \rho V_0^2 L_0/\sigma$ is the Weber number and θ the contact angle (Chandra & Avedisian 1991). To compute this theoretical limit, we take $L_0 = 7.6$ mm, $\rho = 1020$ kg m^{-3} and $\theta = 180°$, which correspond to the lowest values of $L_{max}/L_0|_{cap}$ in our case.

when the suspension concentration increases. This concentration dependance is clear for Carbopol (see also figure 12*a*) but less obvious for clays, for which variations are within the experimental errors at low velocities ($V_0 < 2$ m s^{-1}). In figure 4, we also plot the maximal spread factor predicted when capillarity is the only mechanism that balances the initial kinetic energy (Chandra & Avedisian 1991). All data are well below this capillary limit, suggesting that bulk rheological properties, and not the surface tension, are controlling the arrest of drop spreading in our case. To confirm this hypothesis, we have performed further experiments using super-hydrophobic surfaces.

3.2. *Viscoplastic coating versus giant elastic recoil*

Figure 5 presents a typical dynamical sequence of a kaolin and a Carbopol drop impacting a super-hydrophobic surface at moderate velocity. We first observe that the spreading dynamics are very similar to the one observed on the smooth glass surface. In particular, the maximal drop deformation is identical in both cases. This result is general: as long as impact velocity is not too large, the spreading phase is independent of the impacted surface. For larger velocities, differences arise between the adhesive and non-adhesive surfaces; in particular, on super-hydrophobic surfaces, the splashing transition occurs sooner, and larger maximal deformations are observed (figure 4). We leave this point for future investigations.

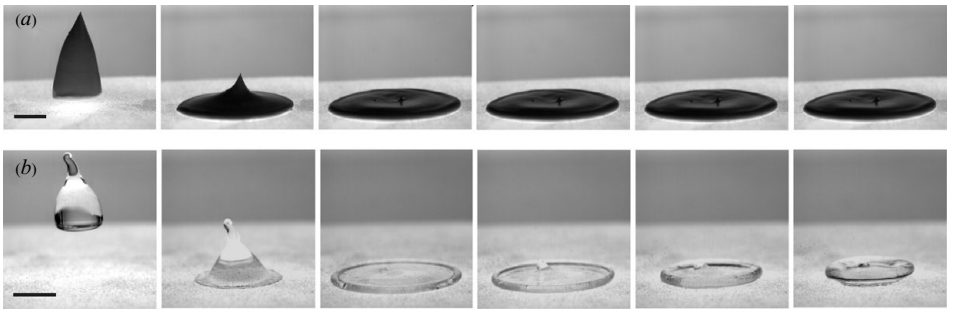

FIGURE 5. (*a*) Viscoplastic coating versus (*b*) giant elastic recoil on a super-hydrophobic surface: (*a*) 55 wt% kaolin drop, time interval between the pictures 7 ms; (*b*) 1 wt% Carbopol drop, time interval between the pictures 6 ms. In both cases, the impact velocity is $V_0 = 2.8$ m s^{-1}. Scale bar, 1 cm.

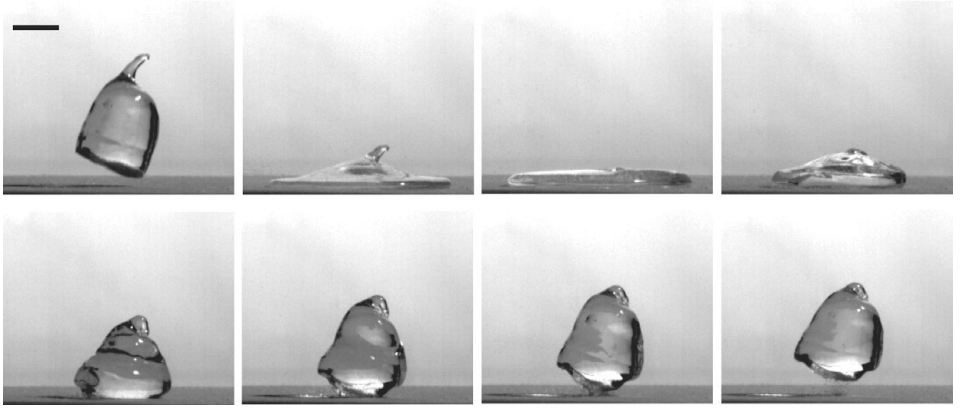

FIGURE 6. Bouncing of a 2 wt% Carbopol drop on a super-hydrophobic surface ($V_0 = 2.4$ m s^{-1}). Time interval between the pictures is 8 ms. Scale bars, 10 mm.

Although the spreading phase weakly depends upon the impacted surface and fluid used, the receding dynamics on super-hydrophobic surfaces reveal striking differences between the clay and Carbopol drops. For clay drops, we observe no receding at all, as shown in figure 5(*a*) (see online movie 1, go to journals.cambridge.org/flm). Once it has reached its maximal extension, the drop maintains its flattened shape and irreversibly coats the plane, even though the surface is super-hydrophobic. This viscoplastic coating is peculiar to yield-stress fluids and confirms that in our cases the flow threshold is high enough to prevent the capillary retraction of the drop. However, impacts with Carbopol drops strongly contrast with this behaviour as shown in figure 5(*b*) (see online movie 2). In this case, after the spreading phase, strong and rapid recoil is always observed, which may even be followed by a complete rebound (figure 6 and online movie 3). A first possibility for this recoiling mechanism is the surface tension, as for Newtonian fluids. However, this is unlikely, since Carbopol drops have yield stresses comparable to those of the clays. A more appealing hypothesis is that Carbopol drops deform and retract elastically, much like a bouncing ball of gel (Tanaka, Yamazaki & Okumura 2003). However, within the range of impact velocity considered, the drop deformations are between 100 % and 500 %, which is much beyond the flow threshold deduced from the steady rheological measurements ($\gamma_c \approx 25\,\%$). This suggests that for Carbopol drops, viscoelastic effects occur: during

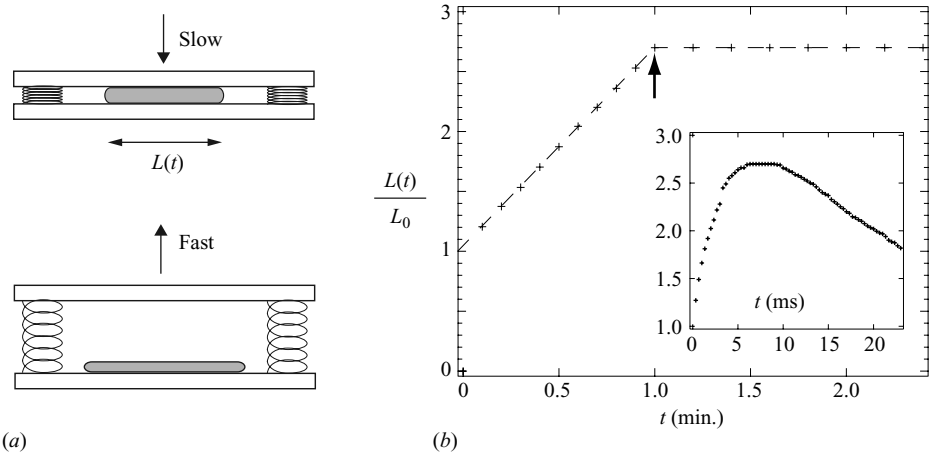

FIGURE 7. (*a*) Sketch of the experiment used to support the viscoelastic behaviour of Carbopol. A drop of Carbopol is quasi-statically squeezed between two super-hydrophobic surfaces and released by suddenly removing the upper plate. (*b*) Time evolution of the diameter of the drop during the experiment. The arrow indicates the sudden motion of the upper plate. For comparison, we give in the inset the dynamics of the same Carbopol drop (1 wt%) impacting a super-hydrophobic surface and reaching an identical maximal spread factor ($V_0 = 2.8$ m s^{-1}).

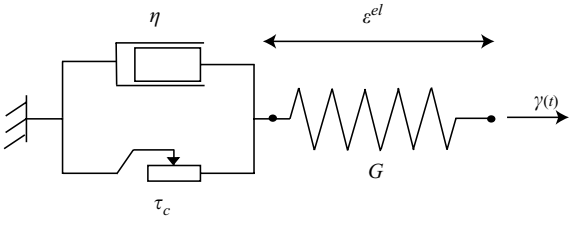

FIGURE 8. Mechanical representation of an elasto-viscoplastic fluid.

the rapid spreading phase, flow is faster than the fluid relaxation time, yielding giant elastic deformations on short time scales.

Further experiments on quasi-static squeezed drops supported this mechanism. To this end, Carbopol drops were slowly compressed between two super-hydrophobic surfaces up to a given spread factor (figure 7*a*). The upper plate was then suddenly removed, and the subsequent dynamics were recorded. We observe that, unlike impinging drops, these flattened drops never retract and keep their final shape (figure 7*b*). This experiment confirms that the surface tension alone cannot overcome the yield stress to recoil the drop. Besides, it highlights the crucial role of viscoelasticity in the case of Carbopol.

A simple mechanical analogue to this elasto-viscoplastic behaviour is presented in figure 8, where the fluid is represented by an elastic spring together with a solid friction and viscous elements in parallel. When displacements $\gamma(t)$ occur on time scales much larger than the relaxation time scale η/G, the response is either purely elastic (below the threshold) or fully viscoplastic (above the threshold). By contrast, when $\gamma(t)$ varies on time scales much shorter than the relaxation time, the response is always dominated by the elastic component, even far beyond the flow threshold. In the following, we extend this simple model to predict the different impact regimes and spreading laws observed.

4. Elasto-viscoplastic model of inertial spreading

Our experimental observations imply that in order to predict the drop impact dynamics for all yield-stress fluids used, both the viscoplasticity and the elasticity of the material have to be taken into account within a time-dependant framework. Our aim in this section is to build a minimal model containing these ingredients. To this end, we will substitute the complex spatio-temporal impact dynamics for a much simpler, purely temporal model, where drop inertia is balanced by an elasto-viscoplastic basal stress inspired by recent works on the rheology of soft materials.

4.1. *Inertial spreading of a shallow disc*

Most theoretical descriptions of Newtonian drops impacting a solid surface rely either on semi-empirical energy balances or on direct numerical simulations (Rein 1993; Yarin 2006). Simplified spatio-temporal models have also been proposed, based on lubrication equations (Yarin 2006) or variational methods (Kim & Chun 2001). To our knowledge, no such model exists in the case of yield-stress fluids.

Here, we consider the simplest time-dependent model of inertial spreading. The drop is modelled by a shallow disc (thickness $h(t)$, radius $R(t)$) that spreads radially along the surface. Assuming the disc aspect ratio to be small (lubrication approximation) and integrating the mass and radial momentum balance across the depth gives (Appendix A)

$$\frac{\mathrm{d}h}{\mathrm{d}t} + 2\frac{Uh}{R} = 0, \tag{4.1}$$

$$\rho h \frac{\mathrm{d}U}{\mathrm{d}t} = -\tau_b, \tag{4.2}$$

where $U \equiv \mathrm{d}R/\mathrm{d}t$ is the front velocity and τ_b is the basal shear stress between the spreading drop and the solid plane. The first equation is the mass conservation for an incompressible disc. The second equation is the radial momentum balance, where the drop inertia is simply balanced by the basal shear stress. Here both the gravity spreading term and the surface tension force arising at the circumferential surface of the disc have been neglected. Those assumptions are reasonable in our case of high Froude numbers and high values of viscosity, yield stress and elasticity compared with the surface tension. We have also neglected any wetting phenomenon, such as hysteresis and dissipation at the contact line, that may affect the receding dynamics. We will return to this point in the conclusion.

Within this simple model, the spreading dynamics are mainly controlled by the expression of the basal shear stress, while the contribution of the radial and hoop stress is neglected. This is valid as long as the spreading drop is thin (lubrication approximation) and does not slip at the solid plane, such that the dominant shear is across the layer. For complex fluids, the no-slip assumption could be addressed, as these fluids often exhibit a slip velocity on smooth surfaces (Meeker *et al.* 2004). However, slip velocities usually reported in yield-stress fluids (about 0.1 mm s^{-1}) are much smaller than the impact velocities (about 1 m s^{-1}). This means that the shear rate at the base scales as $\dot{\gamma} \approx U/h$, which is much larger than the elongation rate U/R in the shallow limit. In the following, we thus assume the shear across the layer to be the dominant mode of the flow and discuss the choice of the basal shear stress, which embodies the fluid rheology.

4.2. *Choice of the rheology*

Constitutive laws for viscoplastic fluids that incorporate elasticity have been the subjects of several studies in the past (e.g. Schwedoff 1890; Tyabin & Trusov 1970; White 1979). Recently, there has been a renewal of such elasto-viscoplastic formulations applied to the rheology of soft disordered materials such as foams, emulsions and gels (Takeshi & Sekimoto 2005; Marmottant & Graner 2007; Saramito 2007; Bénito *et al.* 2008). The most classical way to introduce elasticity in a yield-stress fluid is to suppose a purely elastic behaviour below the yield stress and a purely viscoplastic behaviour above the yield stress (see for example Mujumdar, Beris & Metzner 2002 and the references therein). However, this description does not account for viscoelastic-like effects allowing the material to transiently store large elastic deformations, as observed in our case of drop impacts with Carpobol. To circumvent this, several studies have extended the classical description of viscoelastic fluids used in polymers solutions (Bird *et al.* 1987) to yield-stress materials. The most advanced models are those of Saramito 2007 and Bénito *et al.* 2008. In these approaches, the constitutive law is composed of two parts. First, the stress tensor is given by an elastic law. Secondly, there is a transport equation for the elastic deformation, stipulating that the deformation relaxes only when it is above a critical strain (i.e. a yield stress). These equations constitute a tensorial generalization of the mechanical model given in figure 8. In addition, Saramito's (2007) model is built to recover a Bingham constitutive law in the rigid limit. The great advantage of these full tensorial approaches is that they properly account for nonlinear effects such as finite deformations, elongational flows and normal stresses. They have been applied to simple unidirectional flows, such as uniaxial flows and simple or oscillatory shear flows (Saramito 2007; Bénito *et al.* 2008). However, these are difficult to solve in higher dimensions, even in basic configurations (Cheddadi *et al.* 2008). Moreover, they do not describe the Herschel–Bulkley shear-thinning observed in steady shear with our fluids.

Here we use a simple scalar version of Saramito's (2007) model for the basal shear stress, which we modify in order to recover a Herschel–Bulkley behaviour for steady flows. The basal shear stress τ_b is written as

$$\tau_b = G\epsilon^{el}, \tag{4.3}$$

$$\text{with} \quad \begin{cases} \dfrac{\mathrm{d}\epsilon^{el}}{\mathrm{d}t} = \dot{\gamma} & \text{if } |\epsilon^{el}| < \gamma_c, \\ \qquad = \dot{\gamma} - \dfrac{1}{\lambda}\dfrac{|\epsilon^{el}| - \gamma_c}{|\epsilon^{el}|}\epsilon^{el} & \text{if } |\epsilon^{el}| > \gamma_c. \end{cases} \tag{4.4}$$

The first equation assumes that the basal shear stress is given by an elastic Hooke law, where G is the elastic shear modulus and ϵ^{el} the elastic shear deformation at the base; γ is the total shear strain such that $\gamma = \epsilon^{el} + \epsilon^{vp}$, where ϵ^{vp} is the irreversible (viscoplastic) part of the total deformation. The second equation is a transport equation for the elastic deformation, where $\dot{\gamma} \approx U/h$ is the basal shear rate. It indicates that as long as the elastic deformation is below the critical strain given by $\gamma_c = \tau_c/G$, the fluid behaves like an elastic solid. On the other hand, above the flow threshold, the evolution of the stored elastic deformation is decomposed into an advection term and a creeping term, where λ is a relaxation time scale.

This scalar law constitutes a straightforward extension to shear flows of the mechanical model presented in figure 8. For $\gamma_c = 0$ (no yield stress), one recovers the usual Maxwell model for viscoelastic fluids: $\dot{\tau}_b + (G/\eta)\tau_b = G\dot{\gamma}$, where $\eta \equiv G\lambda$

is the fluid viscosity. On the other hand, for a steady flow ($\mathrm{d}/\mathrm{d}t = 0$, $\epsilon^{el} > \gamma_c$), $\dot{\gamma} = (\epsilon^{el} - \gamma_c)/\lambda$, and the basal shear stress reduces to a simple viscoplastic flow rule: $\tau_b = G\gamma_c + (G\lambda)\dot{\gamma} = \tau_c + \eta\dot{\gamma}$. For a constant relaxation time λ, the viscosity is constant, and one recovers a Bingham flow rule for steady flows (Saramito 2007). However, our fluids exhibit a Herschel–Bulkley behaviour for steady shear flows, such that $\eta = K\dot{\gamma}^{n-1}$. This is possible if the relaxation time satisfies $G\lambda = K((\epsilon^{el} - \gamma_c)/\lambda)^{n-1}$. To be compatible with the Herschel–Bulkley rheology of our fluids in steady shear, we therefore choose the following expression for the relaxation time:

$$\lambda = (K/G)^{1/n}(|\epsilon^{el}| - \gamma_c)^{(n-1)/n} \quad \text{if} \quad |\epsilon^{el}| > \gamma_c, \tag{4.5}$$

where K is the fluid consistency and n is the flow index deduced from steady-state shear measurements. This choice is reminiscent of the White–Metzner model for describing shear-thinning in polymer solutions (Bird *et al.* 1987), where the relaxation time scales as $\lambda = (K/G)\dot{\gamma}^{n-1}$.

The full impact model is therefore given by the mass and momentum equations ((4.7) and (4.8)) together with the elasto-viscoplastic law ((4.3)–(4.5)). To integrate this system of ordinary differential equations, we assume that the drop is initially stress free, $\epsilon^{el}|_0 = 0$, with an initial shape $R|_0 = L_0/2$ and $h|_0 = (2/3)L_0$ (to ensure volume conservation). Assuming that the initial drop vertical velocity is equal to the impact velocity, $\mathrm{d}h/\mathrm{d}t|_0 = V_0$, and using the mass balance (4.7) gives the initial lateral velocity $U|_0 = (R|_0/2h|_0)V_0 = (3/8)V_0$. In the following, we non-dimensionalize the equations using the dimensionless variables

$$R = L_0\hat{R}, \quad h = L_0\hat{h}, \quad t = \frac{L_0}{V_0}\hat{t}, \quad U = V_0\hat{U}. \tag{4.6}$$

After dropping the hats, the dimensionless model is written as

$$\frac{\mathrm{d}h}{\mathrm{d}t} + 2\frac{Uh}{R} = 0, \tag{4.7}$$

$$h\frac{\mathrm{d}U}{\mathrm{d}t} = -\frac{\epsilon^{el}}{M^2}, \tag{4.8}$$

$$\begin{cases} \dfrac{\mathrm{d}\epsilon^{el}}{\mathrm{d}t} = \dfrac{U}{h} & \text{if} \quad |\epsilon^{el}| < \gamma_c, \\ \qquad = \dfrac{U}{h} - \dfrac{1}{De}(|\epsilon^{el}| - \gamma_c)^{1/n}\dfrac{\epsilon^{el}}{|\epsilon^{el}|} & \text{if} \quad |\epsilon^{el}| > \gamma_c, \end{cases} \tag{4.9}$$

$$\epsilon^{el}|_0 = 0, \quad R|_0 = 1/2, \quad h|_0 = 2/3, \quad U|_0 = 3/8, \quad \text{at t} = 0. \tag{4.10}$$

We note that the drop dynamics are entirely governed by three dimensionless numbers, plus n, given by

$$M = \frac{V_0}{\sqrt{G/\rho}}, \quad \gamma_c = \frac{\tau_c}{G}, \quad De = \frac{V_0(K/G)^{1/n}}{L_0}. \tag{4.11}$$

The elastic Mach number M gives the ratio of the impact velocity V_0 to the speed of the elastic shear waves $\sqrt{G/\rho}$. The critical strain γ_c is the ratio of the fluid yield stress to the elastic shear modulus. Finally, the Deborah number De is the ratio of a characteristic fluid relaxation time $(K/G)^{1/n}$ to a characteristic impact time L_0/V_0. In the limit of small Deborah numbers, the elastic deformations relax on time scales much shorter than the impact time, meaning that the flow behaviour is mainly viscoplastic. On the other hand, in the limit of large Deborah numbers, elastic

deformations have no time to relax during the impact. In this case, the behaviour is mainly elastic, even above the flow threshold.

Our model of inertial spreading therefore contains the main physical ingredients that control the drop impact dynamics of a yield-stress fluid: the balance between inertia and bulk stresses, together with an elasto-viscoplastic rheology. However, we emphasize that this purely temporal approach constitutes a very rough simplification of the complex spatio-temporal dynamics observed during the drop impact. In particular, the assumed cylindrical drop shape and the shallow-water hypothesis are not satisfied at early times, where strong thickness gradients and finite aspect ratios occur. Another crude simplification concerns the expression for the basal stress. We estimated all flow fields at the plane in a dimensional way (e.g. $\dot{\gamma} \approx U/h$), without solving the flow within the spreading layer. In addition, when computing the rate of elastic deformations, we have omitted the nonlinear time derivatives (e.g. upper-convected) arising at finite deformations (Bird *et al.* 1987; Saramito 2007; Bénito *et al.* 2008). These points will be briefly addressed in the conclusion.

4.3. *Predicted dynamics and impact regimes*

Before comparing our model with the experimental results, we discuss in this section its main predictions. For simplicity, the flow index is fixed to $n = 0.6$. Figure 9(*a–c*) presents three typical time evolutions of the normalized drop diameter predicted by the model and obtained for different values of the elastic Mach number M, critical strain γ_c and Deborah number De. These dynamics correspond to the three main impact regimes predicted by the model. In figure 9(*a*), the elastic Mach number is small and the critical strain is large, so that the yield stress is never reached during the spreading dynamics ($\gamma = \epsilon^{el}$, $\epsilon^{vp} = 0$). In this case, the drop remains in the solid–elastic regime and undergoes small oscillations about its initial diameter. These oscillations do not decay, since no damping exists in the model below the threshold. At the other extreme, figure 9(*b*) illustrates a large irreversible spreading of the drop obtained when the elastic Mach number is large, the critical strain small and the Deborah number small. In this case, the shear stress far exceeds the yield stress, and most of the initial kinetic energy is dissipated by viscoplasticity ($\gamma \approx \epsilon^{vp} \gg \epsilon^{el}$). The last regime is presented in figure 9(*c*). In this case, the elastic Mach number is large as well, so that the shear stress exceeds the yield stress during the spreading phase. However, the Deborah number is no longer small. As a consequence, the drop no longer stops once it reaches its maximal extension but strongly recoils up to its initial diameter, before oscillating with a smaller amplitude. This situation corresponds to the case in which the spreading time is short compared to the relaxation time, so that elastic deformations dominate the flow even above the yield stress. (In figure 9*c*, the maximal elastic deformation $\epsilon_m^{el} = 270\,\%$ is larger than the irreversible deformation at the maximal drop extension $\epsilon_m^{vp} = 150\,\%$.) This regime is called the liquid–elastic regime in the following. Note that in this case of large elastic recoils, the drop diameter may reach negative values during the receding phase for some parameters. This unphysical prediction of the model results from the lubrication assumption, which neglects the terms that prevent the drop collapsing when $R \to 0$.

A closer investigation of the model shows that the transition between the different regimes are controlled by two important dimensionless groups (figure 9*d*). First, as long as the ratio between the elastic Mach number and the critical strain, $M/\gamma_c = V_0\sqrt{\rho G}/\tau_c$, is below a critical value (solid line in figure 9*d*), the drop is below the flow threshold, and the behaviour is purely elastic (solid-elastic regime). On the other hand, for $M/\gamma_c > 2$, the basal stress overcomes the yield stress during

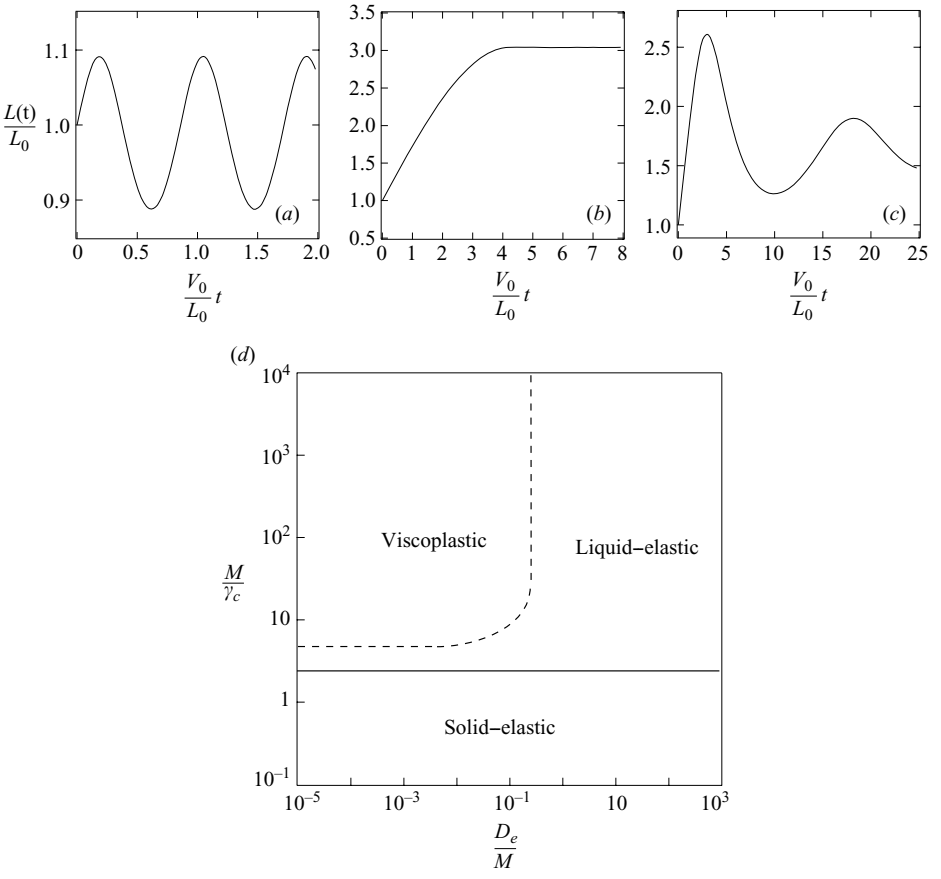

FIGURE 9. Time evolutions of the normalized drop diameter (*a–c*) and impact regimes (*d*) predicted by the model ($n = 0.6$). (*a*) Solid–elastic regime: $M = 0.2$, $\gamma_c = 1$, $De = 0.1$. (*b*) Viscoplastic regime: $M = 1$, $\gamma_c = 0.01$, $De = 10^{-6}$. (*c*) Liquid–elastic regime: $M = 10$, $\gamma_c = 0.1$, $De = 4$. (*d*) The solid line is the solid–liquid transition (below this line, $\epsilon^{vp} = 0$). The dotted line is the boundary between the viscoplastic and liquid–elastic regime given by $\epsilon_m^{el} = \epsilon_m^{vp}$.

the spreading phase. The viscoplastic or liquid–elastic regime observation then depends on the ratio between the Deborah number and the elastic Mach number: $De/M = K^{1/n}/(\rho L_0^2 G^{2-n/n})^{1/2}$. For small De/M, the impact kinetic energy is mostly dissipated by the fluid viscoplasticity, yielding irreversible spreading and coating (viscoplastic regime). By contrast, for large De/M, the drop deformations remain elastic and reversible above the flow threshold due to viscoelastic effects (liquid–elastic regime). In figure 9(*d*), the boundary between the viscoplastic and liquid–elastic regime is plotted for $n = 0.6$ (dotted line). In this case, the boundary does not depend on the value of the critical strain γ_c. For other values of n, the previous discussion remains valid, but the boundary depends upon γ_c (see § 5.1 and figure 11).

Our analysis shows that the transition between the viscoplastic and liquid–elastic regime is essentially controlled by De/M, which does not depend on the impact velocity. This number may be interpreted as the ratio between the viscous relaxation time $(K/G)^{1/n}$ and the elastic mode of vibration of the drop $L_0/\sqrt{G/\rho}$. In this sense, this number is an elastic analogue to the so-called Ohnesorge number $Oh = \eta/(\rho\sigma L_0)^{1/2}$, which compares the viscous damping time to the capillary period

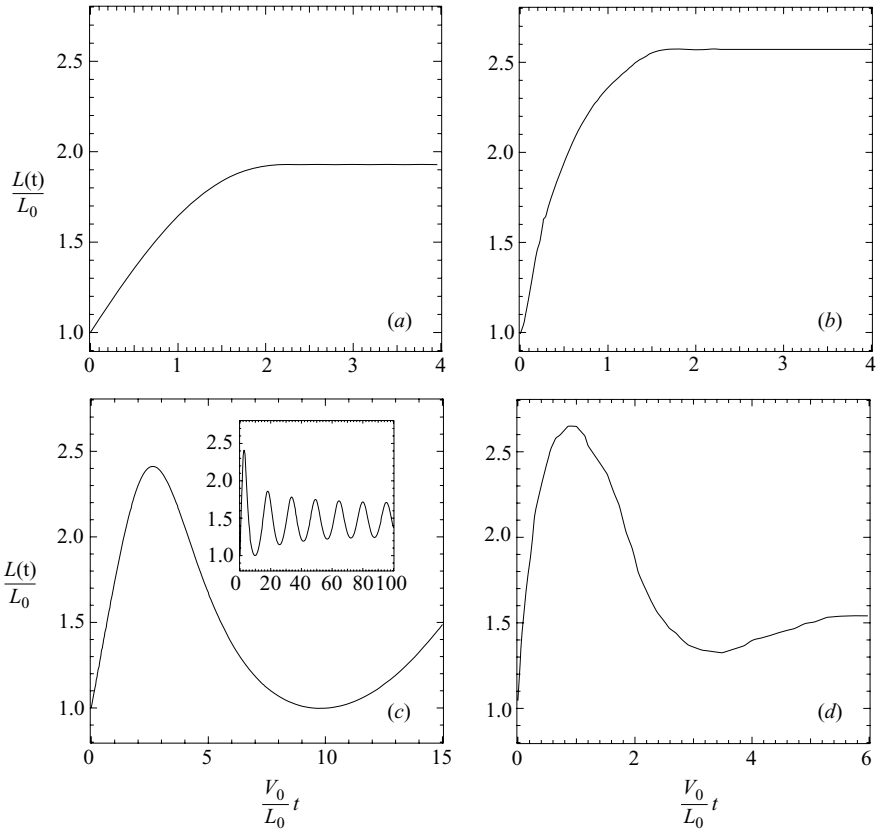

FIGURE 10. Comparison between the spreading dynamics predicted by the model (*a*, *c*) and the experimental measurements (*b*, *d*) for two set of parameters: $M = 0.357$, $\gamma_c = 0.0014$, $De = 3.7\ 10^{-7}$, $n = 0.36$ (*a* and *b*, kaolin 51 wt%, $V_0 = 1.7$ m s^{-1}) and $M = 7.95$, $\gamma_c = 0.28$, $De = 3.26$, $n = 0.5$ (*c* and *d*, Carbopol 1 wt%, $V_0 = 2.3$ m.s^{-1}).

of oscillation of a drop. The Ohnesorge number is well known to play an important role in characterizing the recoiling motion of Newtonian drops (Kim & Chun 2001; Yarin 2006). It is therefore not surprising that De/M plays a similar role for the irreversible coating versus receding transition in our case.

5. Comparison with experiments

In this section, we compare the previous model with the experimental measurements. To this end, the elastic Mach number M, the critical strain γ_c, the Deborah number De and the flow index n introduced in the model are computed from the measured impact velocity V_0 and fluid properties given in table 1. Therefore, no fitting parameter exists when we compare the model with the experimental results.

5.1. *Typical dynamics and phase diagram*

Typical comparisons between the model and the experiments for the spreading dynamics are given in figure 10 for two sets of dimensionless parameters. Experimentally, the first set of parameters corresponds to the impact of a kaolin drop, while the second corresponds to the impact of a Carbopol drop, both measured on the super-hydrophobic surface (to avoid wetting issues not included in the model). The

main result is that the model captures both kinds of dynamics when the experimental values of the dimensionless numbers are introduced in the simulations. For the kaolin case, the drop spreads up to a maximum radius and no longer evolves: all the initial kinetic energy has been dissipated by the viscoplastic friction at the base (figure 10*a*, *b*). By contrast, for the Carbopol drop, strong recoil is predicted and observed (figure 10*c*, *d*). This corresponds to the liquid–elastic regime, where most of the initial kinetic energy has been converted into elastic energy; though the stress far exceeds the yield stress in this case (the maximal total deformation is $\gamma_m \approx 330\,\%$, while the maximal elastic deformation is $\epsilon_m^{el} \approx 220\,\%$, to be compared with the critical strain for Carbopol $\gamma_c = 28\,\%$). Despite this similitude between the model and the experiments, the prediction is not quantitative. In particular, the spreading time is systematically overestimated in the theory. The model also lacks a damping mechanism to suppress the elastic ringing below the flow threshold (figure 10*c*, inset). Nevertheless, the agreement may be regarded as reasonable, considering the simplicity of the model and the fact that no free parameters exists.

In figure 11, we present the phase diagrams predicted by the model for the three kinds of fluids used. In all cases, the solid–liquid transition is the same; however the boundary between the viscoplastic and liquid–elastic regime differs due to different values of γ_c and n. In these diagrams, we also indicate the values of M/γ_c and De/M for all fluids and impact velocities investigated experimentally. We first observe that all experiments (except one) occur above the solid–liquid transition. This means that the impact velocity is always large enough to overcome the yield stress in our experimental conditions. In addition, we observe that kaolin and bentonite drop impacts all belong to the viscoplastic regime, whereas most of the experiments with Carbopol belong to the liquid–elastic regime.

5.2. *Liquid–elastic regime: Carbopol*

The previous phase diagrams suggest that Carbopol impacts are mainly controlled by elasticity. To test this, we present in figure 12 the maximal spread factor measured for Carbopol impacts on the glass surface as a function of the elastic Mach number $M = V_0/\sqrt{G/\rho}$, for all concentrations and impact velocities investigated. The main result is that all data collapse on a master curve. This demonstrates the crucial role of elasticity in the case of Carbopol, even though the flow threshold is greatly exceeded during the impacts. In addition, we observe a rather good quantitative agreement between the model prediction and the experiments.

We can understand the relation between the maximal spread factor and the elastic Mach number M, using simple dimensional arguments and energy conservation. Assuming that the initial kinetic energy is entirely converted into elastic energy, we obtain $\rho L_0^3 V_0^2 \sim G L_0^3 {\epsilon_m^{el}}^2$, where $\epsilon_m^{el} \sim L_m/h$ is the elastic shear strain at the maximal deformation and h the thickness of the maximal drop. Using volume conservation ($L_0^3 \sim h L_m^2$) yields

$$L_m \sim L_0 M^{1/3}. \tag{5.1}$$

The predicted scaling is close to the one obtained experimentally and in the model: $L_m \sim L_0 M^{0.35 \pm 0.01}$ (dashed line in figure 12*b*). The slight difference with the ideal elastic prediction likely results from viscous dissipation. (The Carbopol domain is close to the viscoplastic/liquid–elastic transition; see figure 11.) However, this is difficult to assess owing to the limited range of elastic Mach numbers experimentally accessible.

It is worth noting that the $M^{1/3}$ law is *a priori* valid when the elastic deformations are dominated by the thickness of the drop h, i.e. for a material that adheres to the

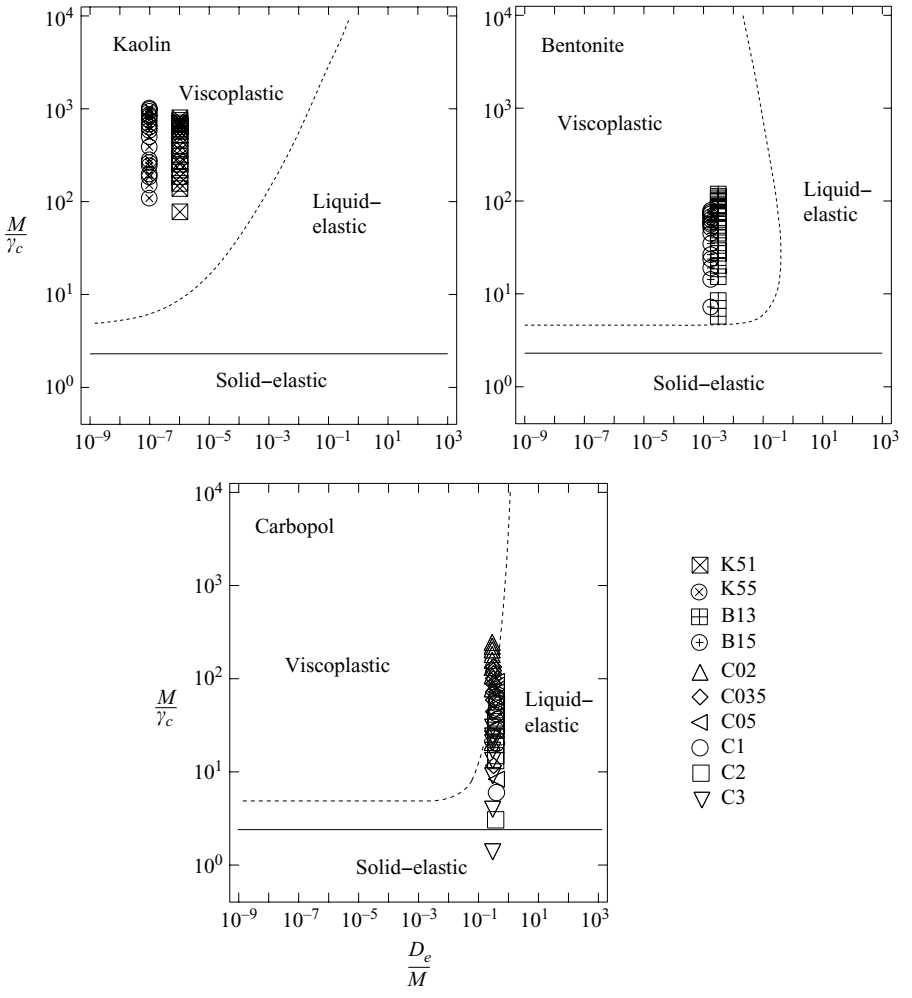

FIGURE 11. Impact regimes predicted by the model in the $(M/\gamma_c$–$De/M)$ plane together with experimental values of M/γ_c and De/M for kaolin, bentonite and Carbopol (symbols). The boundary between the viscoplastic and liquid–elastic regime (dotted line) is computed for each fluid using: $\gamma_c = 0.001$, $n = 0.36$ (kaolin); $\gamma_c = 0.03$, $n = 0.96$ (bentonite); $\gamma_c = 0.25$, $n = 0.5$ (Carbopol).

plane and for large deformations ($M \gg 1$). For smaller deformations ($M \sim 1$) and/or large slip velocity, the elastic deformation should rather scale as $\epsilon_m^{el} \sim (L_m - L_0)/L_0$, yielding $(L_m - L_0)/L_0 \sim M$ (Tanaka *et al.* 2003). Finally, in the low-velocity limit ($M \ll 1$), elastic deformations are localized within the contact area, and impact dynamics strongly depend on the precise geometry of the object (Johnson 1985).

5.3. *Viscoplastic regime: clays*

Unlike Carbopol, experiments with clays and the phase diagrams in figure 11 suggest that during the spreading phase all the initial kinetic energy is irreversibly dissipated. For Newtonian fluids, this 'viscous' regime of spreading is controlled by the Reynolds number, $Re \equiv \rho V_0 L_0/\eta$ (η is the fluid viscosity), and the maximal spread factor is predicted to scale as $L_m \sim L_0 Re^{1/5}$ (Chandra & Avedisian 1991; Rein 1993). In our case, this classical viscous law of spreading should be modified because the fluids are

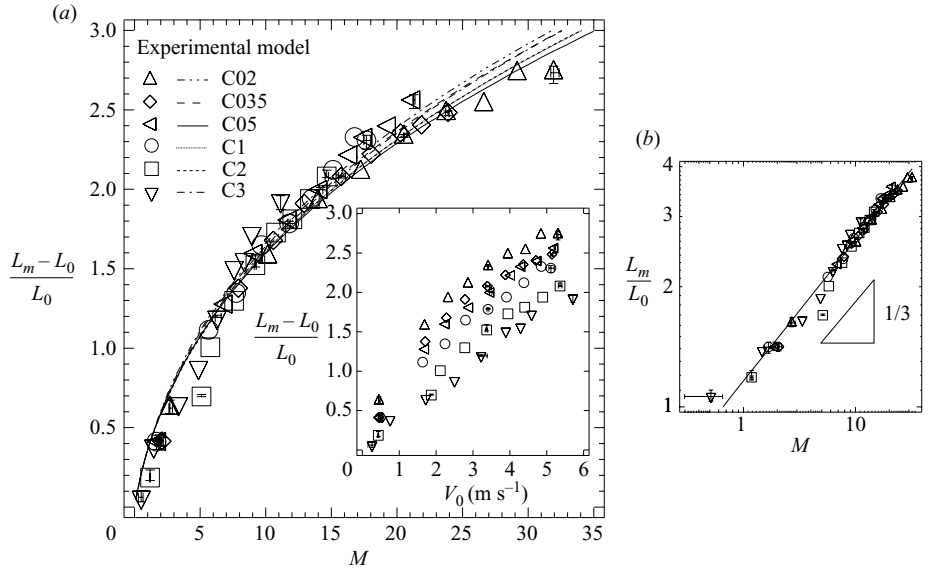

FIGURE 12. (*a*) Relative deformation $(L_m - L_0)/L_0$ versus the elastic Mach number M, for Carbopol drops on glass smooth surface, measured in experiments (symbols) and predicted by the model (lines). Inset : relative deformation as a function of impact velocity. (*b*) Same data for the maximal spread factor versus the elastic Mach number in log–log. The solid line is the experimental data fit giving the law $L_m \sim L_0 M^{0.35 \pm 0.01}$.

shear-thinning above the threshold. Assuming $\eta = K\dot{\gamma}^{n-1} \sim K(V_0/h)^{n-1}$, where h is the thickness of the maximal drop, and using volume conservation ($L_0^3 \sim hL_m^2$) yields

$$L_m \sim L_0 {Re_n}^{1/(2n+3)}, \tag{5.2}$$

where $Re_n \equiv \rho V_0^{2-n} L_0^n / K$ is a generalized Reynolds number.

In figure 13, we present the maximal spread factor as a function of ${Re_n}^{1/(2n+3)}$ for kaolin and bentonite drops, together with previous (see Clanet *et al.* 2004) and new experiments with Newtonian fluids. The main result is that both kaolin and Newtonian fluid data present a straight line of slope 1 in log–log, showing the relevance of the generalized viscous law (5.2). However, they do not collapse on the same curve, the maximal spread factor of kaolin drops being systematically higher ($\sim 25\,\%$) than those of Newtonian drops. A similar discrepancy is obtained when one compares the model predictions to the experiments with kaolin. Again, the model underestimates the spreading by 30 % but predicts the correct scaling law with the generalized Reynolds number. This quantitative difference could result from the model approximations. However, the fact that the model quantitatively agrees with Newtonian fluids suggests a more fundamental explanation. In particular, kaolin viscosity during impact could be actually lower than the one we measured in steady-state rheometry, due to transient effects such as coupling between microstructure orientation and flow (Pignon *et al.* 1997).

The second main observation in figure 13 is that bentonite does not follow the generalized viscous law (5.2). In this case, the velocity dependence of the maximal spread factor ($\sim V_0^{0.50 \pm 0.1}$) is much higher than the one expected for a spreading limited by viscosity ($\sim V_0^{2-n/2n+3} \sim V_0^{0.21}$ with $n = 0.96$). A plausible explanation for this behaviour is that, unlike kaolin, impacts with bentonite are dominated by the yield

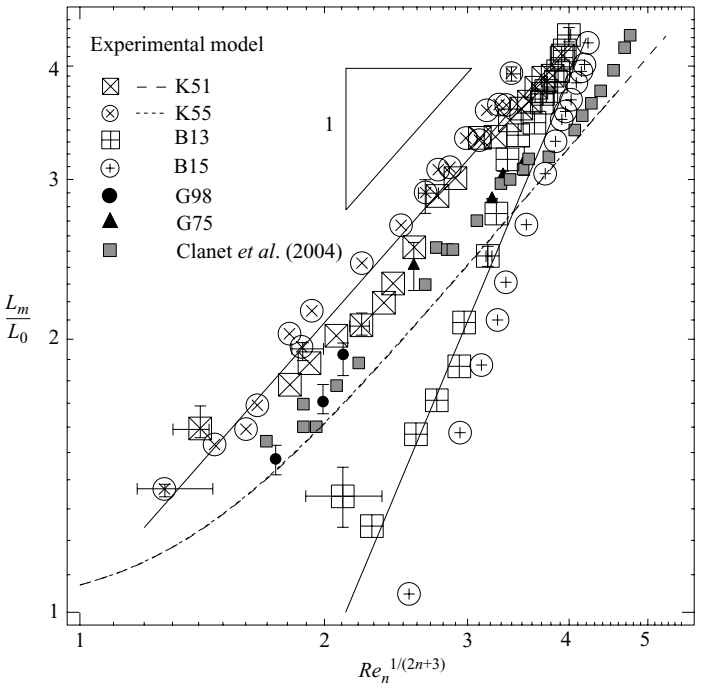

FIGURE 13. Maximal spread factor versus $Re_n^{1/(2n+3)}$, for kaolin and bentonite clays (open symbols) and for Newtonian drops (filled symbols) of two glycerol aqueous solutions concentrated at 75 % ($\eta = 44$ mPa s, G75) and 98 % ($\eta = 472$ mPa s, G98), and results imported from Clanet *et al.* 2004. The dashed lines are the model predictions for the kaolin. The solid lines are power law fit of the experiments for kaolin (slope 1.0 ± 0.05) and bentonite (slope 2.1 ± 0.1).

stress, leading to a shear-rate-independent dissipation mechanism. Such hypothesis is supported by the estimation of the impact Bingham number $Bi \equiv \tau_c L_0^n / K V_0^n$ for both fluids, which compares the yield stress to the typical impact viscous stress. For kaolin drops, we always have $Bi < 0.5$, whereas for bentonite drops $Bi > 3$. For a spreading controlled by the yield stress ('plastic' regime), the maximal spread factor can simply be predicted by balancing the initial kinetic energy with the plastic work (of order $\tau_c L_m^3$), yielding

$$L_m \sim L_0 Y^{2/3}, \tag{5.3}$$

where $Y \equiv V_0 / \sqrt{\tau_c / \rho}$.

The number Y (or its square) is well known in strength-dominated impact of solids and compares the typical impact pressure to the material yield stress (Johnson 1985). In figure 14, we plot the data for bentonite as a function of this new dimensionless number together with the model prediction. The agreement between the model and the experiments is reasonable. Moreover, the spread factor velocity dependence is closer to the ideal plastic regime predicted by (5.3).

We expect the transition between the plastic and viscous regimes to occur when the spread factor predicted by the plastic law (5.3) equates the one given by the viscous law (5.2) (by analogy with the capillary/viscous transition discussed by Clanet *et al.* 2004). This defines a critical velocity $V_c \equiv \tau_c^{(2n+3)/7n} L_0^{3/7} K^{-3/7n} \rho^{-2/7}$ above which the spreading is limited by viscosity and below which it is limited by plasticity. The transition between the plastic and viscous regimes is shown in figure 15, where we

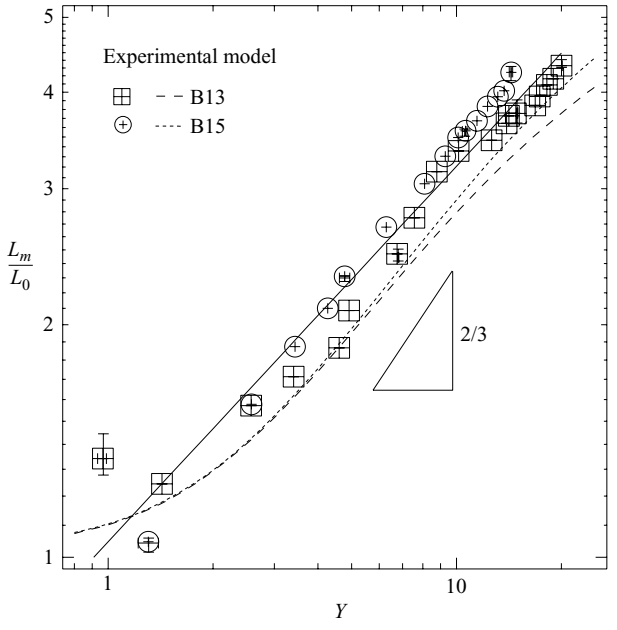

FIGURE 14. Maximal spread factor versus the number $Y \equiv V_0/\sqrt{\tau_c/\rho}$ for bentonite drops, measured (symbols) and predicted (dashed lines). The solid line is the power law fit of the experimental data (slope 0.5 ± 0.1).

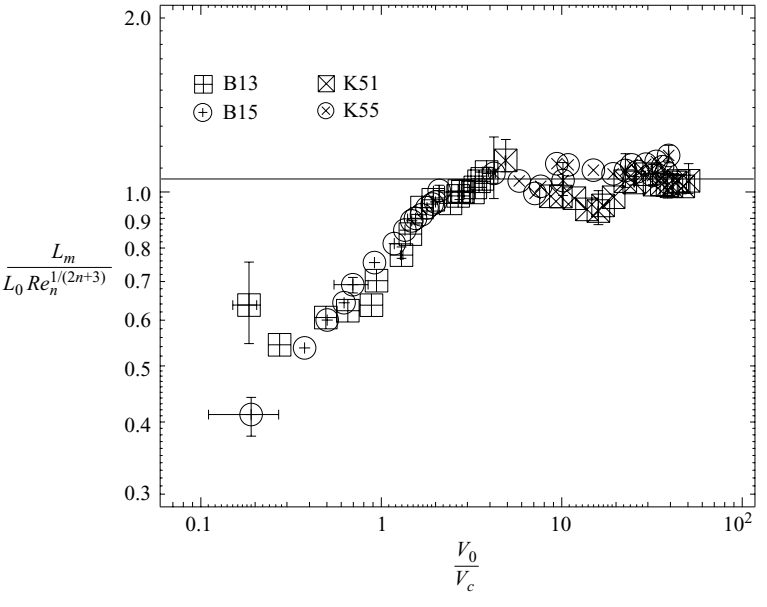

FIGURE 15. Dimensionless viscous extension (where the maximal spreading L_m is normalized by the maximal spreading in the viscous regime $L_0 Re_n{}^{1/(2n+3)}$) versus the impact velocity normalized by the critical viscoplastic velocity V_0/V_c, for kaolin and bentonite drops. The transition occurs for $V_0 \approx 4V_c$.

plot the dimensionless viscous extension $L_m/(L_0 Re_n^{1/(2n+3)})$ as function of V_0/V_c for all experiments with bentonite and kaolin. We observe that the transition is well defined and occurs for $V_0/V_c \approx 4$. As expected, data corresponding to bentonite belong to the plastic regime ($V_0 < 4V_c$), whereas data for kaolin all belong to the viscous regime ($V_0 > 4V_c$).

6. Conclusion

In this paper, the dynamics of drops of yield-stress fluids impacting solid surfaces have been investigated using different model fluids (clay suspensions, Carbopol microgel) and impacted surfaces (partially wetting, super-hydrophobic). We first show that very different impact regimes may be observed, depending on the rheological and mechanical properties of the fluids. For 'stiff' materials (clays), viscoplastic effects dissipate most of the initial kinetic energy during the spreading phase. If the yield stress is large enough to overcome the surface tension, the spreading drop irreversibly coats the surface, irrespective of its wetting property. By contrast, for 'soft viscous' materials (Carbopol), deformations during the impact remain elastic even far above the yield stress, leading to giant elastic spreading and recoil on the super-hydrophobic surfaces. The second main result is that a simple temporal model of spreading combining the drop inertia with an elasto-viscoplastic rheology allows predicting the different regimes observed within a single framework. In addition, semi-quantitative agreements between theory and experiments have been obtained for the maximal spread factor without any fitting parameter, when the measured impact velocity, drop size and fluid rheology were introduced in the model. Our results could therefore be useful to design applications involving the drop impact of yield-stress materials, such as coating processes and solid inkjet printing (Lewis 2006).

Impact experiments with Carbopol have shown that elasticity may play a crucial role in the hydrodynamics of yield-stress fluids, even when the flow deformations are far above the yield stress. This is caused by the highly unsteady flow during the impact, which prevents the elastic deformations to relax. Such viscoelastic-like effects, typical of polymer solutions, are quite difficult to measure for yield-stress fluids in standard rheometers. In this sense, our study of drop impacts has offered a means to probe the short-time rheology of these complex fluids. It is worth noting that the coupling between elasticity and flow deformation is not restricted to transient flows. Normal stresses and extensional viscosity are other consequences of this interplay that could affect the flow of yield-stress fluids in complex configurations. Recent works have begun to investigate this issue in confined geometries (Cheddadi *et al.* 2008). It would be interesting to extend these studies to free surface flows, such as avalanches down inclined planes and free surface instabilities.

Among the different issues raised by our study, the first one concerns the improvement of the model used to describe the drop impact dynamics. Our first approach intended to capture the main physical ingredients. However, it oversimplified the complex spatio-temporal dynamics observed during impact. In particular, the assumed cylindrical drop shape and the shallow-water hypothesis are not valid at early stages, where high vertical velocities and strong thickness gradients are observed. A first improvement of the model could be to split the collapsing drop into a central zone, where the vertical velocity dominates, and a lateral zone, where the shallow-water hypothesis applies (Roisman, Rioboo & Tropea 2002; Larrieu, Staron & Hinch 2006). Another possibility could be to use modified depth-averaged equations that take into account the vertical momentum balance (Boussinesq-type models). However,

all these approaches eventually require the knowledge of the internal velocity field, which may be obtained only by direct numerical simulations. The second improvement concerns the rheology. In this study, we used the simplest elasto-viscoplastic scalar law compatible with a shear-thinning behaviour. However, this approach does not take into account the nonlinear (e.g. upper-convected) derivatives arising in a full tensorial formulation (Bird *et al.* 1987; Saramito 2007). These terms generate a coupling between the shear flow and extensional flow that could strongly affect the impact dynamics. In addition, more complicated choices for the elastic tensor law and the relaxation term could be foreseen (Bénito *et al.* 2008). Finally, we have not considered other rheological features such as thixotropy and coupling between flow and microstructure orientation, which may affect the dynamics of unsteady flows (Coussot *et al.* 2005; Balmforth, Forterre & Pouliquen 2008). Clearly, incorporating all these rheological refinements in a full numerical simulation represents a serious challenge. However, we believe that the relative success of our simple model constitutes an encouragement to test more realistic constitutive laws in precise numerical modelling.

Another question brought up by this study concerns the influence of wetting properties on the interfacial flows of yield-stress fluids. In the beginning of the paper, we suggested that these properties might play a minor role due to the flow threshold. However, our results undermine this assertion. First, the receding dynamics of Carbopol impacts are clearly affected by the wetting properties of the impacted surface. On super-hydrophobic surfaces we observe a strong elastic recoil, whereas on partially wetting surfaces this elastic recoil is inhibited by the contact line dynamics, which remains anchored at the plane. This extra dissipation at the contact line could be enhanced for such a complex fluid due to a subtle interplay between the contact line hysteresis and normal stress differences (Bartolo *et al.* 2007). Secondly, we observe that the spreading dynamics at high impact speeds are also affected by the wetting properties of the impacted surface. Besides promoting the splashing transition as in classical Newtonian fluids, impacts on super-hydrophobic surfaces show a striking phenomenon with Carbopol: above a critical speed, the spread factor becomes much larger than on the glass surface. To our knowledge, this behaviour has never been reported with Newtonian fluids, for which the impact spread factor is unaffected by the use of textured hydrophobic surfaces (Clanet *et al.* 2004). Is this 'super-spreading' the signature of a giant slip velocity between the yield-stress fluid and the super-hydrophobic surface? Does it result from the stabilization of the splashing instability due to viscoelastic effects? We will address these questions in a future work.

Finally, it would be interesting to extend the present study to yield-stress fluid impacts on soft surfaces made of the same material. In this case, both the projectile and the hitting ground may liquefy during the collision, before solidifying again once the kinetic energy is dissipated. This behaviour is reminiscent of impact crater formation in geophysics or in ballistic impact, although other phenomena such as heating, melting and fracture complicate the picture (Melosh 1989). Assuming an impacting body of size $L_0 \approx 1$ km and speed $V_0 \approx$ 1 km s^{-1} striking a surface planet of density $\rho \approx 3000$ kg m^{-3}, yield-strength $\tau_c \approx 10^7$ Pa, Young modulus $G \approx 10^9$ Pa and viscosity $\eta \approx 10^9$ Pa s (Melosh 1989) gives an elastic Mach number $M \approx 20$, a critical strain $\gamma_c \approx 10^{-2}$ and a Deborah number $De \approx 1$. In this study, we have seen that such parameters are easily obtained with standard yield-stress fluids. Investigating the hydrodynamics of crater formation with those materials could therefore help to get insight into the complex process of impact cratering in planetary science.

We thank Pierre Philippe (CEMAGREF, Aix-en-Provence) for providing us the kaolin clay and Jean-Michel Perret who performed several preliminary measurements. It is also a pleasure to thank Pascale Aussilous, Guillaume Chambon, Sergey Gavrilyuk, Assia Ghemmour, Guillaume Ovarlez, Olivier Pouliquen and Pierre Saramito for enlightening discussions.

Appendix A. Derivation of the inertial spreading model

The axisymmetric Saint-Venant mass and momentum conservation equations for an incompressible flow read (without gravity and surface tension)

$$\frac{\partial h}{\partial t} + \frac{1}{r}\frac{\partial ruh}{\partial r} = 0, \tag{A 1}$$

$$\rho\left(\frac{\partial hu}{\partial t} + \frac{1}{r}\frac{\partial rhu^2}{\partial r}\right) = -\tau_b, \tag{A 2}$$

where $h(r,t)$ is the local thickness, $u(r,t)$ the depth-averaged velocity and τ_b the basal shear stress (de Saint-Venant 1871; Witham 1974; Larrieu *et al.* 2006). The main assumption to derive these equations is that the drop aspect ratio h/R is small (shallow-water hypothesis). This allows to neglect both the inertial pressure terms and the radial and hoop stresses. In addition, the acceleration term is simplified assuming $(1/h)\int_0^h \tilde{u}^2(r,z,t)\mathrm{d}z \approx u^2(r,t)$, where $\tilde{u}(r,z,t)$ is the depth velocity profile. In this paper, we model the spreading drop by a disc of radius $R(t)$ and uniform thickness $h(t)$. In this case, the mass conservation equation implies (since there is no divergence of velocity at $r=0$)

$$u(r,t) = -\frac{r}{2h}\frac{\mathrm{d}h}{\mathrm{d}t}. \tag{A 3}$$

Substituting this expression into the Saint-Venant equations (A 1)–(A 2) at $r=R(t)$ yields

$$\frac{\mathrm{d}h}{\mathrm{d}t} + 2\frac{hU}{R} = 0, \tag{A 4}$$

$$\rho h\frac{\mathrm{d}U}{\mathrm{d}t} = -\tau_b, \tag{A 5}$$

where $U = u(R(t),t)$ is the front velocity.

REFERENCES

Awerbuch, N. J. & Bodner, S. R. 1974 Experimental investigation of normal perforation of projectile in metallic plates. *Intl J. Solids Struct.* **10**, 685–699.

Balmforth, N. J., Forterre, Y. & Pouliquen, O. 2009 The viscoplastic Stokes layer. *J. Non-Newton. Fluid Mech.* **158**, 46–53.

Balmforth, N. J. & Frigaard, I. 2007 Viscoplastic fluids: from theory to application. *J. Non-Newton. Fluid Mech.* **142**, 1–244.

Barnes, H. A., Hutton, J. F. & Walters, K. 1989 *An Introduction to Rheology*. Elsevier.

Bartolo, D., Boudaoud, A., Narcy, G. & Bonn, D. 2007 Dynamics of non-Newtonian droplets. *Phys. Rev. Lett.* **99**, 174502.

Bénito, S., Bruneau, C.-H., Colin, T., Gay, C. & Molino, F. 2008 An elasto-visco-plastic model for immortal foams or emulsions. *Eur. Phys. J.* E **25**, 225–251.

Bird, R. B., Armstrong, R. C. & Hassager, O. 1987 *Dynamics of Polymeric Liquids: Fluid Mechanics*, vol. 1. John Wiley.

Bussmann, M., Chandra, S. & Mostaghimi, J. 2000 Modeling the splash of a droplet impacting a solid surface. *Phys. Fluids* **12**, 3121–3132.

de Bruyn, J. R., Habdas, P. & Kim, S. 2002 Fingering instability of a sheet of yield-stress fluid. *Phys. Rev.* E **66**, 031504.

Chambon, G., Ghemmour, A. & Laigle, D. 2009 Gravity-driven surges of a viscoplastic fluid: an experimental study. *J. Non-Newton. Fluid Mech.* **158**, 54–62.

Chandra, S. & Avedisian, C. T. 1991 On the collision of a droplet with a solid surface. *Proc. R. Soc. Lond.* A **432**, 13–41.

Cheddadi, I., Saramito, P., Raufaste, C., Marmottant, P. & Graner, F. 2008 Numerical modelling of foam Couette flows. *Eur. Phys. J.* E **432**, 123–133.

Clanet, C., Béguin, C., Richard, D. & Quéré, D. 2004 Maximal deformation of an impacting drop. *J. Fluid Mech.* **517**, 199–208.

Cooper-White, J. J., Crooks, R. C. & Boger, D. V. 2002 A drop impact study of worm-like viscoelastic surfactants solutions. *Colloids Surf.* A **210**, 105–123.

Coussot, P. 1994 Steady, laminar, flow of concentrated mud suspension in open channel. *J. Hydraul. Res.* **32**, 535–559.

Coussot, P. 2005 *Rheometry of Pastes, Suspensions and Granular Materials.* Wiley Interscience.

Coussot, P. & Gaulard, F. 2005 Gravity flow instability of viscoplastic materials: The ketchup drip. *Phys. Rev.* E **72**, 031409.

Coussot, P., Roussel, N., Jarny, S. & Chanson, H. 2005 Continuous or catastrophic solid–liquid transition in jammed systems. *Phys. Fluids* **17**, 011704.

Crossland, B. 1982 *Explosive Welding of Metals and Its Applications.* Oxford Science.

Johnson, K. L. 1985 *Contact Mechanics.* Cambridge University Press.

Kim, H.-Y. & Chun, J.-H. 2001 The recoiling of liquid droplets upon collision with solid surfaces. *Phys. Fluids* **13**, 643–659.

Larrieu, E., Staron, L. & Hinch, E. J. 2006 Raining into shallow water as a description of the collapse of a column of grains. *J. Fluid Mech.* **554**, 259–270.

Lewis, J. A. 2006 Direct ink writing of three-dimensional functional materials. *Adv. Funct. Mater.* **16**, 2193–2204.

Magnin, A. & Piau, J. M. 1990 Cone-and-plate rheometry of yield stress fluids: study of an aqueous gel. *J. Non-Newton. Fluid Mech.* **36**, 85–108.

Marmottant, P. & Graner, F. 2007 An elastic, plastic, viscous model for slow shear of a liquid foam. *Eur. Phys. J.* E **23**, 337–347.

Meeker, S. P., Bonnecaze, R. T. & Cloitre, M. 2004 Slip and flow in soft particle pastes. *Phys. Rev. Lett.* **92**, 198302.

Melosh, H. J. 1989 *Impact Cratering: A Geologic Process.* Oxford University Press.

Mohamed Abdelhaye, Y. O., Chaouche, M. & Van Damme, H. 2008 The tackiness of smectite muds. Part 1. The dilute regime. *Appl. Clay Sci.* **42**, 163–167.

Mujumdar, A., Beris, A. N. & Metzner, A. B. 2002 Transient phenomena in thixotropic systems. *J. Non-Newton. Fluid Mech.* **102**, 157–178.

Nigen, S. 2005 Experimental investigation of the impact of an (apparent) yield-stress material. *Atom. Sprays* **15**, 103–117.

O'Brien, V. T. & Mackay, M. 2002 Shear and elongation flow properties of kaolin suspensions. *J. Rheol.* **46**, 557–572.

van Olphen, H. 1977 *An Introduction to Clay Colloid Chemistry*, 2nd edn. Wiley.

Oppong, F. K., Rubatat, L., Friskein, B. J., Bailey, A. E. & de Bruyn, J. R. 2006 Microrheology and structure of a yield-stress polymer gel. *Phys. Rev.* E **73**, 041405.

Osmond, D. I. & Griffiths, R. W. 2001 The static shape of yield strength fluids slowly emplaced on slopes. *J. Geophys. Res.* **106**, 16241–16250.

Peixinho, J., Nouar, C., Desaubry, C. & Théron, B. 2005 Laminar transitional and turbulent flow of yield stress fluid in a pipe. *J. Non-Newton. Fluid Mech.* **128**, 172–184.

Piau, J. M. 2007 Carbopol gels: elastoviscoplastic and slippery glasses made of individual swollen sponges; meso-and macroscopic properties, constitutive equations and scaling laws. *J. Non-Newton. Fluid Mech.* **144**, 1–29.

Pignon, F., Magnin, A. & Piau, J.-M. 1996 Thixotropic colloidal suspensions and flow curves with minimum: identification of flow regimes and rheometric consequences. *J. Rheol.* **40**, 573–587.

Pignon, F., Magnin, A. & Piau, J.-M. 1997 Butterfly light scattering pattern and rheology of a sheared thixotropic clay gel. *Phys. Rev. Lett.* **79**, 4689–4692.

Rein, M. 1993 Phenomena of liquid drop impact on solid and liquid surfaces. *Fluid. Dyn. Res.* **12**, 61–93.

Renardy, Y., Popinet, S., Duchemin, L., Renardy, M., Zaleski, S., Josserand, C., Drumwright-Clarke, M. A., Richard, D., Clanet, C. & Quéré, D. 2003 Pyramidal and toroidal water drops after impact a solid surface. *J. Fluid Mech.* **484**, 69–83.

Rieber, M. & Frohn, A. 1999 A numerical study of the mechanism of splashing. *Intl J. Heat Fluid Flow* **20**, 455–461.

Roisman, I. V., Rioboo, R. & Tropea, C. 2002 Normal impact of a liquid drop on dry surface: model for spreading and receding. *Proc. R. Soc. Lond.* A **458**, 1411–1430.

de Saint-Venant, A. J. C. 1871 Théorie du mouvement non-permanent des eaux, avec application aux crues des rivières et à l'introduction des marées dans leur lit. *C. R. Acad. Sci. Paris* **73**, 147–154.

Saramito, P. 2007 A new constitutive equation for elastoviscoplastic fluid flows *J. Non-Newton. Fluid Mech.* **145**, 1–14.

Schwedoff, T. 1890 Experimental researches on the cohesion of liquids. Part 2. Viscosity of liquids. *J. Phys.* **9**, 34–46.

Tabuteau, H., Coussot, P. & de Bruyn, J. R. 2007 Drag force on a sphere in steady motion through a yield-stress fluid. *J. Rheol.* **51**, 125–137.

Tanaka, Y., Yamazaki. Y. & Okumura, K. 2003 Bouncing gel balls: impact of soft gels onto rigid surface. *Europhys. Lett.* **63**, 149–155.

Takeshi, O. & Sekimoto, K. 2005 Internal stress in a model elastoplastic fluid. *Phys. Rev. Lett.* **95**, 108301.

Thoroddsen, S. T. & Sakakibara, J. 1998 Evolution of the fingering pattern of an impacting drop. *Phys. Fluids* **10**, 1359–1373.

Tyabin, N. V. & Trusov, S. A. 1970 Theory of the flow of an elastoviscoplastic medium. *J. Engng Thermophys.* **18**, 716–723.

White, J. L. 1979 A plastic-viscoelastic constitutive equation to represent the rheological behaviour of concentrated suspensions of small particles in polymer melts *J. Non-Newton. Fluid Mech.* **5**, 177.

Witham, G. B. 1974 *Linear and Nonlinear Waves.* Wiley Interscience.

Xu, L., Zhang, W. W. & Nigel, S. R. 2005 Drop splashing on a dry smooth surface. *Phys. Rev. Lett.* **94**, 184505.

Yarin, A. L. 2006 Drop impact dynamics: splashing, spreading, receding, bouncing ... *Annu. Rev. Fluid. Mech.* **38**, 159–192.

Yarin, A. L., Rubin, M. B. & Roisman, I. V. 1995 Penetration of a rigid projectile into an elastic-plastic target of finite thickness. *Intl J. Impact Engng* **16**, 801–831.

Yarin, A. L., Zussman, E., Theron, A., Rahimi, S., Sobe, Z. & Hasan D. 2004 Elongational behaviour of gelled propellant simulants. *J. Rheol.* **48**, 101–116.

Yoshitake, Y., Mitani, S., Sakai, K. & Takagi, K. 2008 Surface tension and elasticity of gel studied with laser-induced surface deformation spectroscopy. *Phys. Rev.* E **78**, 041405.